Electronic Supplementary Material (ESI) for Chemical Science.

Supporting Information

Experimental Section

Synthesis and crystal growth: Bi_2O_3 (Aladdin, 99.0%), H_2mdap (Aladdin, 98%), and Hydrogen Bromide (HBr, Aladdin, 48 wt.%) were purchased and used without further purification. The growth procedure is schematically illustrated in **Figure 1b** with a facile solvent evaporation method. Bi_2O_3 (2.347 g, 5 mmol) and H_2mdap (0.232 g, 5 mmol) were dissolved in 20 mL HBr solution with continuous stirring at the heating platform. A yellow solution was obtained after the solutes were completely dissolved. After several days, the desired bulk SCs with a size of centimeters were obtained.

Photoelectric measurements. A laser diode with wavelength of 404 nm (L404P400M, Thorlabs) was used for the light source. The voltage vs time (*V*-*t*) was measured using a highly accurate electrometer (Keithley 6517B) with a controlled temperature of 298 K using a Linkam TS1500 heating stage.

X-Ray Detection. The current-voltage (*I*-*V*) traces and current-time (*I*-*t*) curves of 1 SC device were recorded by a Keithley 6517B high-precision electrometer. An Amptek Mini-X2 X-ray tube with the silver target (maximum power 4 W) was used as the X-ray source. A silicon detector calibrates the radiation dose rate. The X-ray energy is up to 50 keV and the peak intensity is at 22 keV.

Calculations of Sensitivity (*S*) and Signal-to-Noise Ratio (*SNR*). *S* can be determined by,

$$S = (I_{x\text{-}ray} - I_d)/(D \times A) \quad \text{.....(S1)}$$

where $I_{x\text{-ray}}$ and I_d are the currents recorded under X-ray irradiation and in the dark, respectively, *D* is the irradiation dose rate, and *A* is the effective area of the detector.

SNR is calculated by [1, 2],

$$SNR = \frac{I_{signal}}{I_{noise}} = \frac{T_{x\text{-}ray} - T_d}{\sqrt{\frac{1}{n}\sum_{1}^{n}(I_i - T_{x\text{-}ray})^2}} \quad \text{..... (S2)}$$

where I_{signal} is the signal current, I_{noise} is the noise current, $T_{x\text{-}ray}$ is the average device current under X-ray irradiation, T_d is the average dark current, n is the number of parallel experiments under each bias.

Calculations of theoretical Sensitivity (*S**). *S** can be determined by,

$$S^* = \frac{e}{W_{\pm} \times (\frac{\mu_{en}}{\rho})} \quad \text{.....(3)}$$

$$W_{\pm} = 2.8 \times bandgap + 0.5(eV) \quad \text{.....(4)}$$

where *e* is the elementary charge, $\frac{\mu_{en}}{\rho}$ is the mass energy-absorption coefficient in the air of the maximum X-ray energy of 50 keV and the peak intensity of 22 keV (**Figure S9a**), obtained from the NIST database. (**Figure S9b**), $W_{\pm}$ is the amount of radiation energy consumed per electron-hole pair generated in a semiconductor. [3] Bandgap refers to the bandgap of the response material, in $[H_2mdap]BiBr_5$ case, it is 2.94 eV (**Figure S9c**).

Calculation of Dark Current Drift (I_{drift}). The dark current drift is calculated using the following equations,

$$E = \frac{V}{d} \quad \text{..... (S5)}$$

$$I_{drift} = (I_t - I_0)/(E \times S \times t) \quad \text{..... (S6)}$$

in which *V*, *d*, I_0, I_t, *E*, and *S* are the bias, this distance between the two Ag electrodes, the current immediately after stabilization, the current at time *t*, the electric field, and the device area, respectively.

Figures

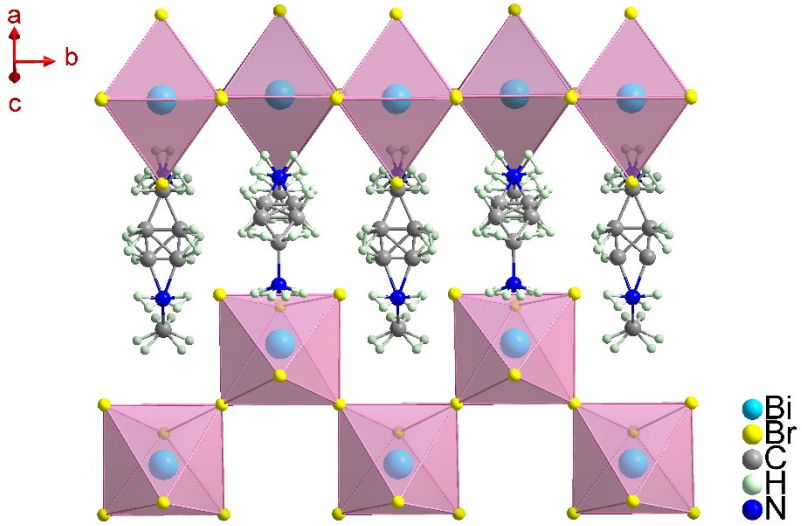

Figure S1. The crystal structure of **1** at the paraelectric phase.

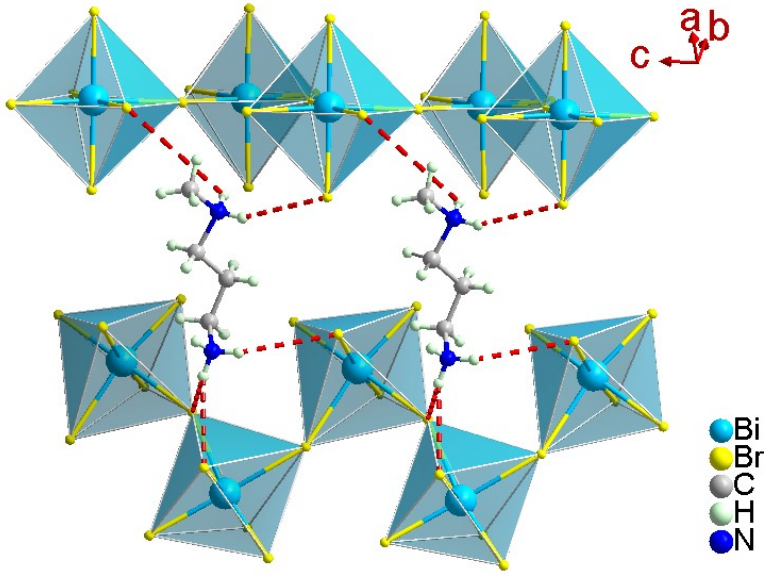

Figure S2. N–H···Br hydrogen bonds (dash lines) between organic cations and inorganic skeletons.

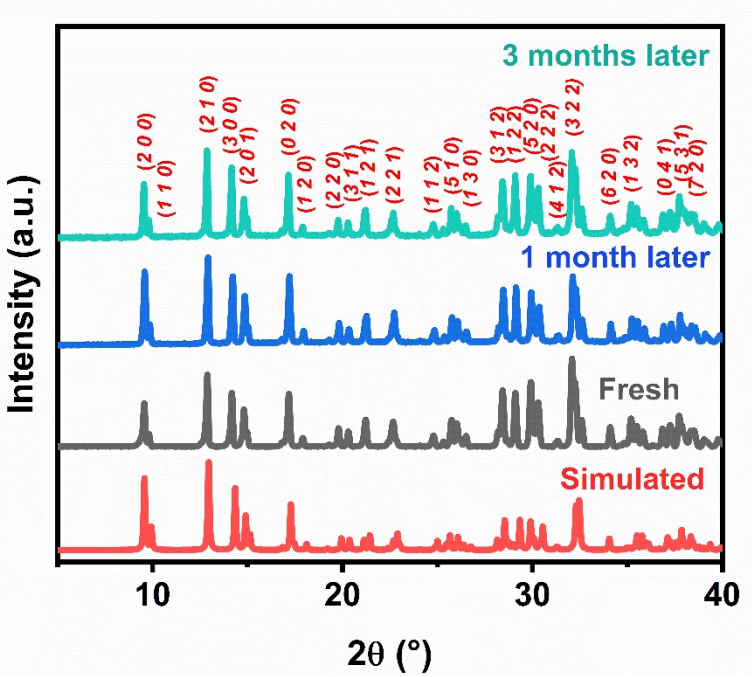

Figure S3. Powder X-ray diffraction patterns of **1**, verify its environmental stability.

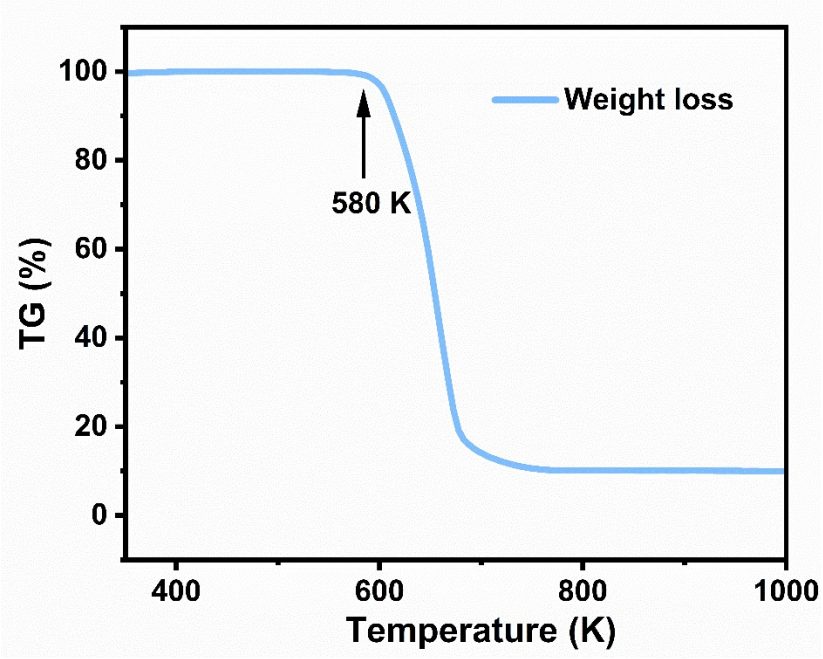

Figure S4. TG curve of **1** powder.

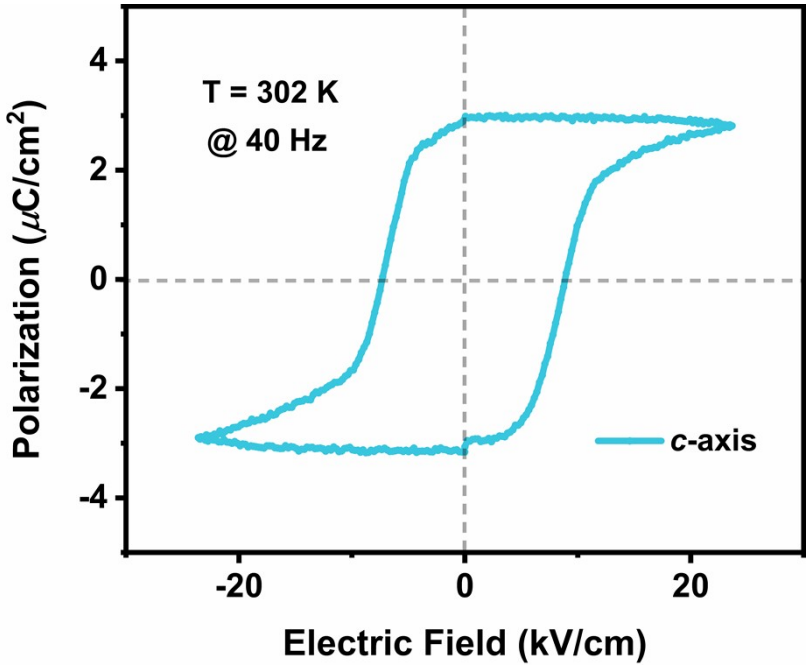

Figure S5. Polarization electric field hysteresis loop of **1**.

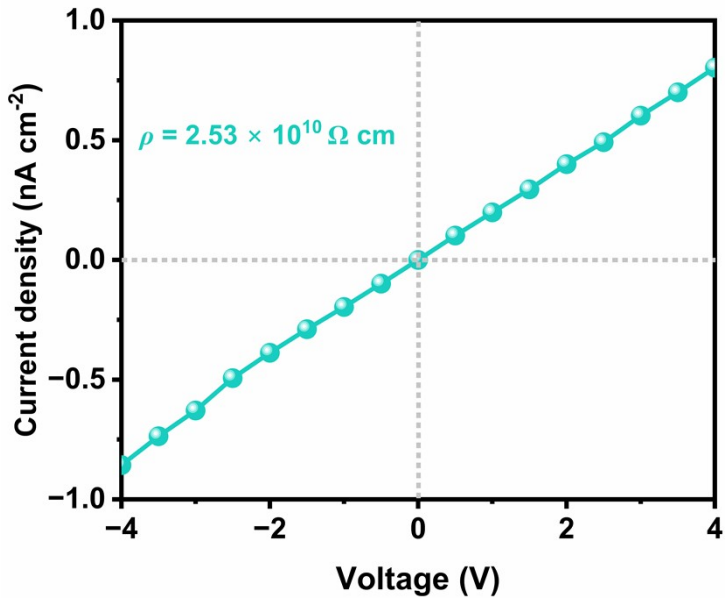

Figure S6. Bulk resistivity of the **1** SC.

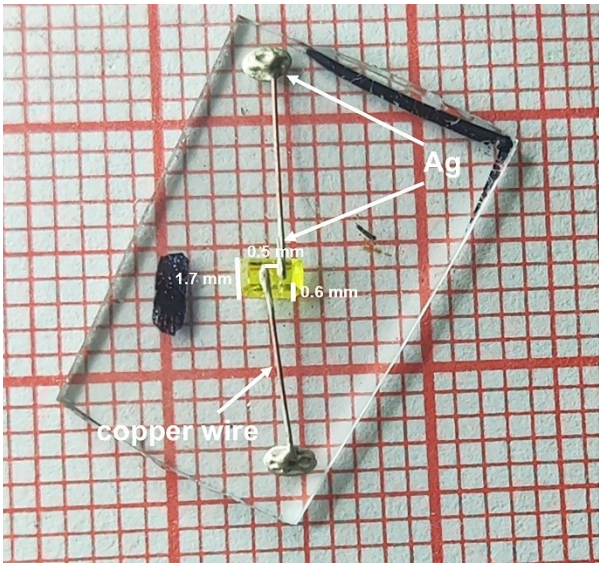

Figure S7. The single-crystal device of **1**.

The planar structure photodetectors were assembled using the single-crystal devices of samples. Two symmetric Ag electrodes were coated on the flat side of the bulk single crystal. Subsequently, the above-obtained electrode was placed on the glass sub-strate for the measurement.

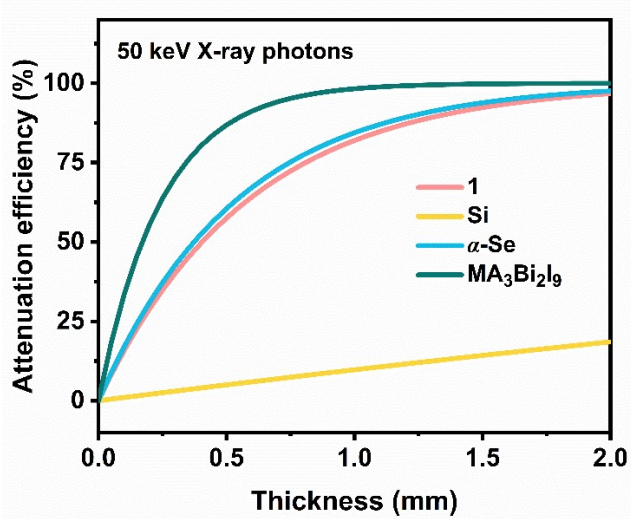

Figure S8. Attenuation efficiencies of **1**, Si, α-Se, and $MA_3Bi_2I_9$ for 50 keV X-ray photons versus thickness.

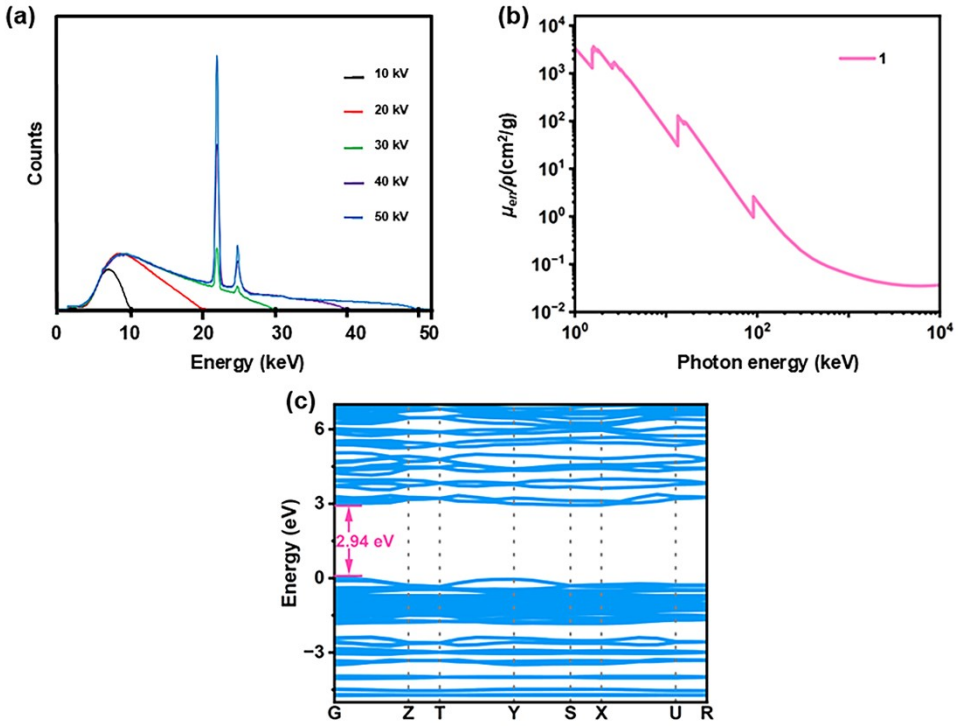

Figure S9. a) The Mini-X2 Silver (Ag) Output Spectrum at 10, 20, 30, 40, 50 kV; b) the X-ray mass energy-absorption coefficient in air, obtained from the NIST database; c) The calculated band structure of **1**.

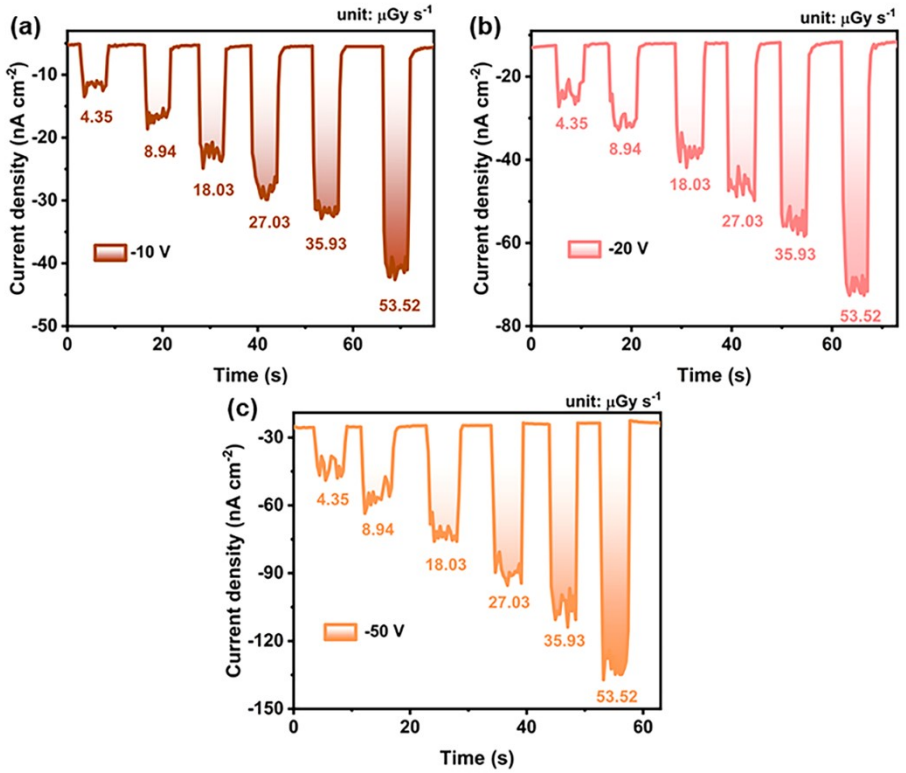

Figure S10. *I-t* curves of **1** SC detector under increased X-ray dose rates at -10, -20, and -50 V bias.

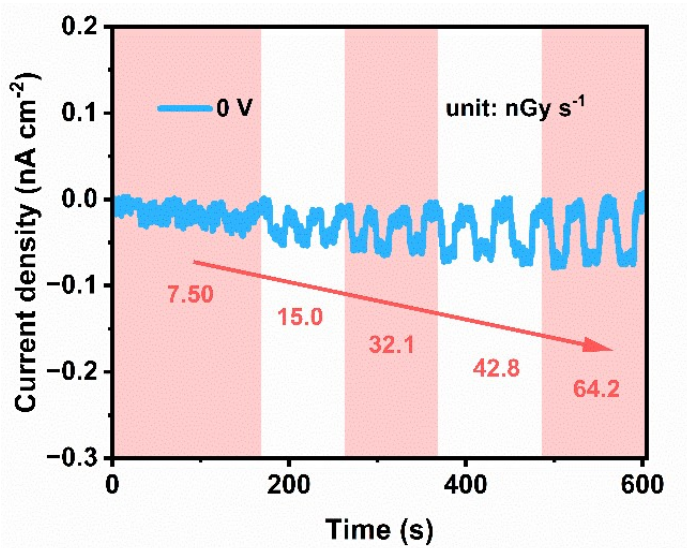

Figure S11. Photoresponses of **1** detector to X-ray under increased dose rates at zero bias.

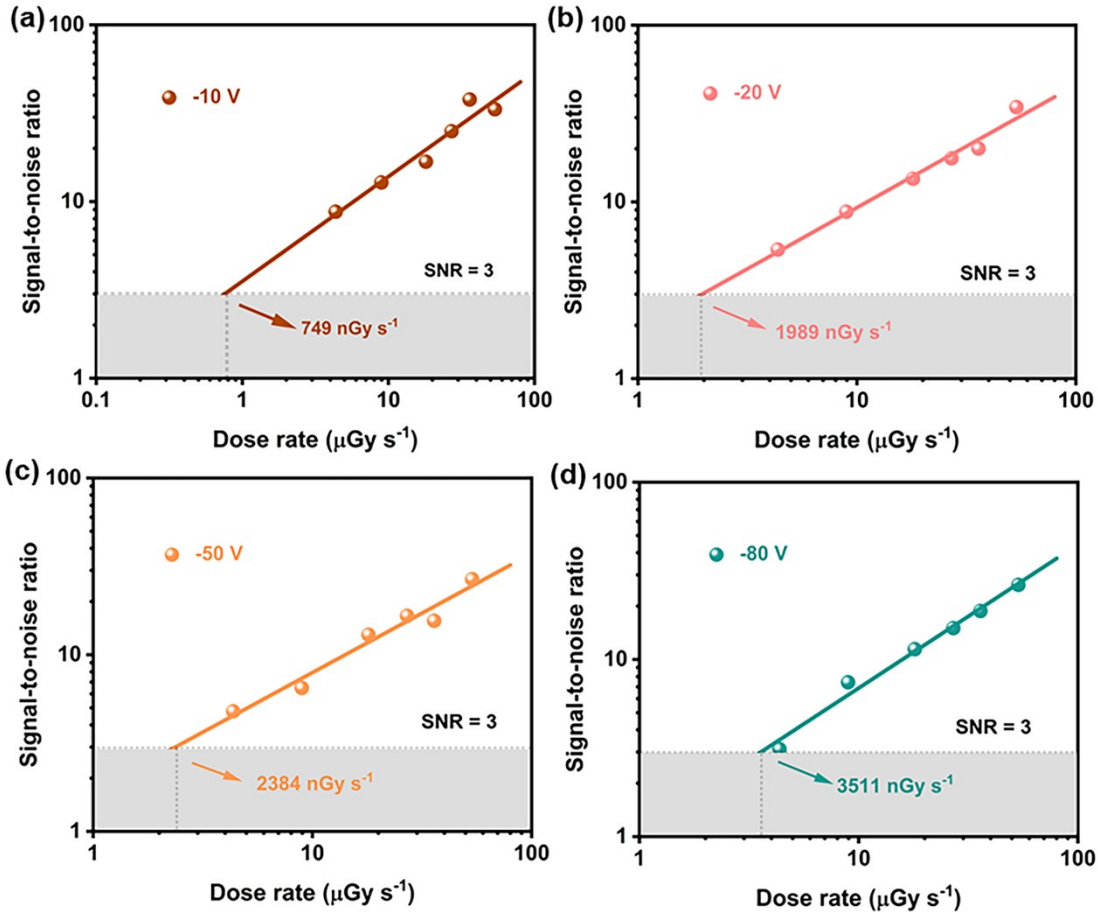

Figure S12. SNRs of **1** detector under different dose rates at -10, -20, -50, and -80 V bias, which derives the LoD of 749, 1989, 2384, and 3511 nGy s^{-1}, respectively.

Table S1. Comparison of sensitivity and detection limit of Pb-free perovskite single crystal X-ray detectors.

Materials	Dimensionality	detection limit (nGy s^{-1})	Sensitivity (μC Gy^{-1} cm^{-2})	Operating voltage (or electric field)	X-ray Energy (keV)	Ref.
(*R*-MPA)$_4$AgBiI$_8$	2D	85	46.3	0 V	22	4
		547	949.6	50 V		
$(NH_4)_3Bi_2I_9$	2D	<55(⊥)	803(⊥)	6.5 V mm^{-1}	/	5
(I-BA)$_4$AgBiI$_8$	2D	/	5.38	10 V	80	6
[(*S*-PPA)$_4$(IPA)$_6$Ag$_2$Bi$_4$I$_{24}$]·2H$_2$O	2D	129.5	42.8	3 V mm^{-1}	/	7
(CPA)$_4$AgBiBr$_8$ (ferroelectricity)	2D	/	0.8	10 V	70	8
(HIS)$_2$AgSbBr$_8$	2D	84.2	123	10 V	/	9
(DFPIP)$_4$AgBiI$_8$ (ferroelectricity)	2D	3130	188	50 V	29	10
PEA-Cs$_2$AgBiBr$_6$	2D	/	288.8	22.7 V mm^{-1}	/	11
(FPEA)$_4$AgBiBr$_8$	2D	2600	27	333V mm^{-1}	/	12
(*R*)-(H$_2$MPz)BiI$_5$	1D	4350	263.58	50 V mm^{-1}	/	13
(BAH)BiI$_4$	1D	77	1181.8	50 V	40	14
(DMEDA)BiI$_5$	1D	/	1.6	5 V	50	15
(PDA)BiBr$_5$	1D	/	~3.8	100 V	50	16
(4-AMP)BiI$_5$	1D	482	66.84	0 V	22	17
		806	1139.74	50 V		
(HDA)BiI$_5$ (ferroelectricity)	1D	266	170.7	0 V	/	18

$(MA)_3Bi_2I_9$	0D	83	1974	60 V mm^{-1}	40	19
$(Gua)_3Bi_2I_9$	0D	145	7.44	1 V	70	20
$(R\text{-PPA})_2BiI_5$	0D	270	31	0 V	22	21
		2370	150	10 V		
$FA_3Bi_2I_9$	0D	200	598	555 V mm^{-1}	45	22
$(R\text{-MPz})_6Bi_3I_{21}\cdot 6H_2O$	0D	4350	5.2	0 V	/	23
$(HIS)BiI_5$	0D	36	1000	10 V	/	24
$(BZA)_2(R\text{-PPA})BiI_6$	0D	18.5	53.2	0 V	/	25
$(MA_{0.7}Cs_{0.3})_3Bi_2I_9$	0D	12.8@60 V	130@90 V	/	/	26
$(DGA)BiI_5\cdot H_2O$	0D	4.7	5879.4	100 V mm^{-1}	40	27
$[H_2mdap]BiBr_5$ (ferroelectric)	**1D**	**28**	**79**	**0 V**	**22**	**This work**
		3511	**2618.7**	**-80 V**		

Reference

1 Y. Hua, G. Zhang, X. Sun, P. Zhang, Y. Hao, Y. Xu, Y. Yang, Q. Lin, X. Li, Z. Zhai, F. Cui, H. Liu, J. Liu, X. Tao, *Nat. Photonics.* 2024, **18**, 870-877.

2 M. Li, H. Li, W. Li, B. Li, T. Lu, X. Feng, C. Guo, H. Zhang, H. Wei, B. Yang, *Adv. Mater.* 2022, **34**.

3 C. A. Klein, *J. Appl. Phys.* 1968, **39**, 2029-2038.

4 J. Wu, S. You, P. Yu, Q. Guan, Z.-K. Zhu, Z. Li, C. Qu, H. Zhong, L. Li, J. Luo, *ACS Energy Lett.* 2023, **8**, 2809.

5 R. Zhuang, X. Wang, W. Ma, Y. Wu, X. Chen, L. Tang, H. Zhu, J. Liu, L. Wu, W. Zhou, X. Liu, Y. M. Yang, *Nat. Photonics.* 2019, **13**, 602.

6 Z. Xu, H. Wu, D. Li, W. Wu, L. Li, J. Luo, *J. Mater. Chem. C.* 2021, **9**, 13157.

7 Z.-K. Zhu, T. Zhu, J. Wu, S. You, P. Yu, X. Liu, L. Li, C. Ji, J. Luo, *Adv. Funct. Mater.* 2023, **33**, 2214660.

8 W. Guo, X. Liu, S. Han, Y. Liu, Z. Xu, M. Hong, J. Luo, Z. Sun, *Angew Chem Int Ed.* 2020, **59**, 13879.

9 Q. Fan, H. Xu, S. You, Y. Ma, Y. Liu, W. Guo, X. Hu, B. Wang, C. Gao, W. Liu, J. Luo, Z. Sun, *Small.* 2023, **19**, 2301594.

10 C.-F. Wang, H. Li, M.-G. Li, Y. Cui, X. Song, Q.-W. Wang, J.-Y. Jiang, M.-M. Hua, Q. Xu, K. Zhao, H.-Y. Ye, Y. Zhang, *Adv. Funct. Mater.* 2021, **31**, 2009457.

11 W. Yuan, G. Niu, Y. Xian, H. Wu, H. Wang, H. Yin, P. Liu, W. Li, J. Fan, *Adv. Funct. Mater.* 2019, **29**, 1900234.
12 M. Ge, S. Chen, X. Fu, Y. Feng, D. Wang, M. Yuan, *J. Phys. Chem. C* 2022, **126**, 19417-19423.
13 X. Dong, J. Liang, Z. Xu, H. Wu, L. Wang, S. You, J. Luo, L. Li, *Chin. Chem. Lett.* 2023, 108708.
14 C. Ma, H. Li, M. Chen, Y. Liu, K. Zhao, S. F. Liu, *Adv. Funct. Mater.* 2022, **32**, 2202160.
15 L. Yao, G. Niu, L. Yin, X. Du, Y. Lin, X. Den, J. Zhang, J. Tang, *J. Mater. Chem. C.* 2020, **8**, 1239.
16 Y. Xu, J. Hu, X. Du, X. Xiao, M. Li, J. Tang, J. Chen, Y. He, *Chem Asian J.* 2021, **16**, 4137.
17 S. You, P. Yu, T. Zhu, C. Lin, J. Wu, Z.-K. Zhu, C. Zhang, Z. Li, C. Ji, J. Luo, *Adv. Funct. Mater.* 2023, 2310916.
18 D. Fu, Y. Ma, S. Wu, L. Pan, Q. Wang, R. Zhao, X. M. Zhang, J. Luo, *ACS Appl. Mater. Interfaces.* 2024. DOI: 10.1002/inf2.12602.
19 Y. Liu, Z. Xu, Z. Yang, Y. Zhang, J. Cui, Y. He, H. Ye, K. Zhao, H. Sun, R. Lu, M. Liu, M. G. Kanatzidis, S. F. Liu, *Matter.* 2020, **3**, 180-196.
20 Y. Xu, J. Hu, X. Xiao, H. He, G. Tong, J. Chen, Y. He, *Inorg. Chem. Front.* 2022, **9**, 494.
21 S. You, Z.-K. Zhu, S. Dai, J. Wu, Q. Guan, T. Zhu, P. Yu, C. Chen, Q. Chen, J. Luo, *Adv. Funct. Mater.* 2023, **33**, 2303523.
22 W. Li, D. Xin, S. Tie, J. Ren, S. Dong, L. Lei, X. Zheng, Y. Zhao, W.-H. Zhang, *J. Phys. Chem. Lett.* 2021, **12**, 1778.
23 X. Dong, T. Chen, J. Liang, L. Wang, H. Wu, Z. Xu, J. Luo, L.-N. Li, *Chin. J. Struct. Chem.* 2024, 100256.
24 Z. Zhao, Q. Fan, Y. Liu, H. Rong, H. Ni, L. Wei, X. Zhao, J. Luo, Z. Sun, *ACS Appl. Mater. Interfaces.* 2024, **16**, 38283-38289.
25 Z.-K. Zhu, T. Zhu, S. You, P. Yu, J. Wu, Y. Zeng, Q. Guan, Z. Li, C. Qu, H. Zhong, L. Li, J. Luo, *Small* 2023, **20**, 2307454.
26 S. Tie, D. Xin, S. Dong, B. Cai, J. Zhu, X. Zheng, *ACS Sustainable Chem. Eng.* 2022, **10**, 10743-10751.
27 B. Zhang, Y. Zhang, H. Su, E. Huang, Z. Zhao, Z. Xu, Y. Liu, L. Zhang, Z. Zeng, J. You, A. K. Y. Jen, S. Liu, *Small* 2024, 2405071.